INVITED PAPER *Special Section on Coding and Coding Theory-Based Signal Processing for Wireless Communications*

Spatially Coupled LDPC Coding and Linear Precoding for MIMO Systems*

Zhonghao ZHANG[†a)], **Chongbin XU**[†], ***and*** **Li PING**[†], ***Nonmembers***

SUMMARY In this paper, we present a transmission scheme for a multiple-input multiple-output (MIMO) quasi-static fading channel with imperfect channel state information at the transmitter (CSIT). In this scheme, we develop a precoder structure to exploit the available CSIT and apply spatial coupling for further performance enhancement. We derive an analytical evaluation method based on extrinsic information transfer (EXIT) functions, which provides convenience for our precoder design. Furthermore, we observe an area property indicating that, for a spatially coupled system, the iterative receiver can perform error-free decoding even the original uncoupled system has multiple fixed points in its EXIT chart. This observation implies that spatial coupling is useful to alleviate the uncertainty in CSIT which causes difficulty in designing LDPC code based on the EXIT curve matching technique. Numerical results are presented, showing an excellent performance of the proposed scheme in MIMO fading channels with imperfect CSIT.

key words: *spatial coupling, linear precoding, MIMO, LDPC code, linear minimum mean-square error, message passing detection, EXIT chart*

1. Introduction

The extrinsic information transfer (EXIT) chart analysis technique [1]–[5] has been widely used for the design of low-density parity-check (LDPC) codes and turbo codes with iterative decoding [6]–[8]. With this technique, near capacity performance can be approached by matching the EXIT curves of two local processors (decoders) of an iterative receiver in an additive white Gaussian noise (AWGN) channel [3], [5].

For a multiple-input multiple-output (MIMO) system with perfect channel state information at the transmitter (CSIT), the channel can be transformed into a set of parallel subchannels using singular value decomposition (SVD). The MIMO capacity can then be achieved by independent coding for each sub-channel, following the water-filling principle [9]. The design problem in this case is similar to that for an AWGN channel.

For a *quasi-static* MIMO channel without CSIT, however, the optimal design for the transmitter remains a challenging problem. In this case, it is difficult to apply the EXIT curve matching technique. (See Fig. 5 for this issue.) This problem becomes more complicated when the available CSIT is imperfect, containing both useful information as well as errors. In this case, to the best of our knowledge, even the outage capacity of the system is still unknown and the optimal transmitter design problem remains open [10].

Detection complexity is another issue, especially for MIMO systems with a large number of antennas. Among different options, linear minimum mean-square error (LMMSE) [11] detection has suboptimal performance but relatively low complexity. Techniques that can improve the performance of MIMO systems with LMMSE detection are thus highly desirable.

In this paper, we will first consider the transmission issues for MIMO systems without CSIT. We focus on a linear precoding technique that can facilitate LMMSE detection. We develop an analytical EXIT curve method to evaluate the performance of MIMO systems with LDPC coding and linear precoding. We apply the spatial coupling approach [12]–[14] to treat the EXIT curve mismatching problem. We show that, with spatial coupling, an iterative decoder can converge to the correct detection even when the two EXIT curves have multiple fixed points. This leads to a noticeable performance improvement.

We will then extend our discussions to MIMO systems with partial (imperfect) CSIT. We propose a heuristic precoding scheme that works efficiently with partial CSIT. Spatial coupling is again used to deal with the EXIT curve mismatching problem. Numerical results demonstrate that the proposed scheme can achieve impressive gain (relative to the case of no CSIT). This provides an attractive solution to practical MIMO systems.

2. System Model

Consider a flat-fading MIMO system with M_R receive antennas and M_T transmit antennas. Denote by $\boldsymbol{H}(n)$ the $M_R \times M_T$ channel matrix and $\boldsymbol{y}(n)$ the transmitted sequence of length M_T at time slot n. The received sequence of length M_R is given by

$$\boldsymbol{r}(n) = \boldsymbol{H}(n)\boldsymbol{y}(n) + \boldsymbol{z}(n) \tag{1}$$

where $\boldsymbol{z}(n)$ denotes a complex AWGN sequence of length M_R with zero mean and covariance matrix $N_0\boldsymbol{I}$.

For convenience of the discussion, we consider the following extended system model over N time slots

$$\boldsymbol{r} = \boldsymbol{H}\boldsymbol{y} + \boldsymbol{z} \tag{2}$$

Manuscript received July 6, 2012.
Manuscript revised August 22, 2012.

[†] The authors are with the Department of Electronic Engineering, City University of Hong Kong, Hong Kong SAR, P.R. China.

[*] This work has been performed in the framework of the FP7 project ICT-248894 WHERE2 (Wireless Hybrid Enhanced Mobile Radio Estimators-Phase 2) which is partly funded by the European Union.

a) E-mail: zhozhang@student.cityu.edu.hk

DOI: 10.1587/transcom.E95.B.3663

where $\boldsymbol{H}$ is an $NM_R \times NM_T$ block diagonal matrix with N diagonal submatrices, i.e.,

$$\boldsymbol{H} = \mathrm{diag}\,(\boldsymbol{H}(1), \ldots, \boldsymbol{H}(N)) \tag{3}$$

and $\boldsymbol{y}$ is a length-NM_T transmitted sequence

$$\boldsymbol{y} = \left[\boldsymbol{y}^T(1), \ldots, \boldsymbol{y}^T(N)\right]^T. \tag{4}$$

The other sequences $\boldsymbol{r}$ and $\boldsymbol{z}$ are defined similarly.

To make the discussion simpler, we assume that the channel is time-invariant over N time slots, i.e., $\boldsymbol{H}(n) = \boldsymbol{H}'$ for $1 \leq n \leq N$. The extension to the time-varying fading case is straightforward.

To characterize the CSIT, we consider the following channel mean information (CMI) model [10], [15]

$$\boldsymbol{H} = \sqrt{\alpha}\overline{\boldsymbol{H}} + \sqrt{1-\alpha}\boldsymbol{H}_W \tag{5}$$

where $\overline{\boldsymbol{H}}$ and $\boldsymbol{H}_W$ are $NM_R \times NM_T$ block diagonal matrices, representing the known and unknown parts of $\boldsymbol{H}$ at the transmitter. The entries of the diagonal submatrices of $\boldsymbol{H}_W$ are modeled as independent and identically distributed (i.i.d.) complex Gaussian random variables with zero mean and unit variance. The CSIT quality is measured by α ($0 \leq \alpha \leq 1$): $\alpha = 0$ for no CSIT and $\alpha = 1$ for perfect CSIT.

For simplicity, we first discuss the no CSIT case ($\alpha = 0$) in Sects. 3, 4, and 5, and then discuss the precoder design in the partial CSIT case ($\alpha > 0$) in Sect. 6.

3. Transmitter and Receiver Structure

3.1 Linear Precoding without CSIT

Figure 1(a) illustrates the transmitter structure and the channel, where $\boldsymbol{y}$ is generated by a linear precoder as

$$\boldsymbol{y} = \boldsymbol{P}\boldsymbol{x}. \tag{6}$$

Here $\boldsymbol{P}$ denotes an $NM_T \times NM_T$ precoding matrix and $\boldsymbol{x}$ is a symbol sequence of length NM_T generated by an LDPC encoder. The power of each symbol is assumed to be normalized.

Without CSIT (i.e., $\alpha = 0$), we adopt the following linear precoder structure developed in [16]

$$\boldsymbol{P} = \boldsymbol{\Pi}\boldsymbol{F} \tag{7}$$

where $\boldsymbol{\Pi}$ and $\boldsymbol{F}$ are, respectively, an $NM_T \times NM_T$ random permutation matrix and an $NM_T \times NM_T$ Hadamard matrix. This precoder structure provides diversity advantage [16].

Denote by $\boldsymbol{A} = \boldsymbol{H}\boldsymbol{P}$ the equivalent $NM_R \times NM_T$ channel matrix. From (2) and (6), we have

$$\boldsymbol{r} = \boldsymbol{A}\boldsymbol{x} + \boldsymbol{z}. \tag{8}$$

Figure 1(b) illustrates a factor graph representation [17], [18] of the block diagram in Fig. 1(a), where each circle represents a variable node and each square represents a check node.

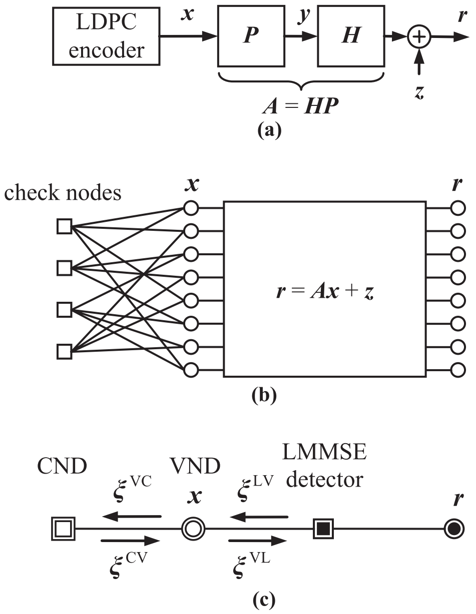

Fig. 1 (a) Transmitter structure. (b) Factor graph of the transmitter. (c) A concise form of the factor graph in (b).

Figure 1(b) can be redrawn in a more concise form as shown in Fig. 1(c), where each node (a double circle or a double square) represents multiple nodes in Fig. 1(b). Accordingly, each edge in Fig. 1(c) represents multiple edges in Fig. 1(b). This concise factor graph provides convenience for our discussions below.

3.2 Message Passing Detection Algorithm

The symbol sequence $\boldsymbol{x}$ in Fig. 1(c) satisfies two constraints which are imposed, respectively, by the linear system in (8) and by the LDPC code.

At the receiver, message passing detection algorithm [17], [18] is adopted based on the above two constraints. This is illustrated in Fig. 1(c), where the concise factor graph represents the receiver structure. There are three local detectors, namely, an LMMSE detector, a variable node detector (VND), and a check node detector (CND). The LMMSE detector recovers the symbol sequence $\boldsymbol{x}$ based on the linear constraint in (8), while the CND and VND decode the symbol sequence $\boldsymbol{x}$ based on the LDPC coding constraint. They exchange messages following the turbo principle [8] as shown in Fig. 1(c), where each message is a sequence consisting of log-likelihood ratios (LLRs). We use superscripts to distinguish these messages. For example, the message from the LMMSE detector to the VND is denoted by $\boldsymbol{\xi}^{\mathrm{LV}}$. The other three messages are distinguished similarly.

3.3 LMMSE Detection

For convenience, we assume binary phase shift keying (BPSK) [19] for the coded symbols in $\boldsymbol{x}$. The discussion can be extended to other modulation methods [20].

Assume that the LLR message $\boldsymbol{\xi}^{\mathrm{VL}} = \{\xi_m^{\mathrm{VL}}\}$ of length

NM_T has been generated and passed to the LMMSE detector as shown in Fig. 1(c). (We will return to this issue in 3.5.) We can generate the LMMSE detection outputs $\boldsymbol{\xi}^{\text{LV}} = \{\xi_m^{\text{LV}}\}$ of length NM_T as follows.

Compute the *a priori* mean and variance of x_m as [21]

$$\overline{x}_m = \tanh(\xi_m^{\text{VL}}/2) \text{ and } v_m = 1 - \overline{x}_m^2. \tag{9}$$

Letting

$$v_m \approx \overline{v} = \frac{1}{NM_T}\sum_{n=1}^{NM_T} v_n \tag{10}$$

we can obtain the LMMSE estimate of $\boldsymbol{x}$ as [11]

$$\hat{\boldsymbol{x}} = \overline{\boldsymbol{x}} + \overline{v}\boldsymbol{A}^H\boldsymbol{R}^{-1}(\boldsymbol{r} - \boldsymbol{A}\overline{\boldsymbol{x}}) \tag{11}$$

where $\overline{\boldsymbol{x}} = \{\overline{x}_m\}$, and $\boldsymbol{R} = \overline{v}\boldsymbol{A}\boldsymbol{A}^H + N_0\boldsymbol{I}$.

The *extrinsic* LLR of x_m is given by (see Appendix)

$$\xi_m^{\text{LV}} = 2\left(\Omega_{m,m}^{-1}\hat{x}_m - \overline{v}^{-1}\overline{x}_m\right) \tag{12}$$

where $\Omega_{m,m}$ is the m-th diagonal entry of the mean-square error (MSE) matrix [11]

$$\boldsymbol{\Omega} = \overline{v}\boldsymbol{I} - \overline{v}^2\boldsymbol{A}^H\boldsymbol{R}^{-1}\boldsymbol{A}. \tag{13}$$

We write the LMMSE detection outputs as $\boldsymbol{\xi}^{\text{LV}} = \{\xi_m^{\text{LV}}\}$, which are passed to the VND as shown in Fig. 1(c).

3.4 Modeling the LMMSE Detection Outputs

The LMMSE detection outputs can be modeled as the observations from an equivalent AWGN channel. It is shown that when the precoder matrix $\boldsymbol{F}$ in (7) is properly chosen, ξ_m^{LV} can be expressed as [c.f., (5), (17) and (18) in 21]

$$\xi_m^{\text{LV}} = \mu x_m + \varepsilon_m \tag{14}$$

where μ is a constant with respect to m, and ε_m is an independent Gaussian random variable with zero mean and variance σ^2.

Define the signal-to-noise ratio (SNR) for (14) as $\rho^{\text{LV}} \equiv \mu^2/\sigma^2$. We have [c.f., (16c) in 16]

$$\rho^{\text{LV}} = \phi(\overline{v}) \equiv \left(\frac{1}{NM_T}\text{trace}\left(\frac{1}{\overline{v}}\boldsymbol{I} + \frac{\boldsymbol{A}^H\boldsymbol{A}}{N_0}\right)^{-1}\right)^{-1} - \frac{1}{\overline{v}}. \tag{15}$$

3.5 VND/CND Operations and Overall Iterative Process

Based on (14), we can regard the LMMSE detection outputs as the observations from an equivalent AWGN channel. The messages $\boldsymbol{\xi}^{\text{VC}}$ and $\boldsymbol{\xi}^{\text{CV}}$ between the CND and VND are generated based on the standard message passing algorithm [4], [5]. The details are omitted here. Furthermore, the message $\boldsymbol{\xi}^{\text{VL}} = \{\xi_m^{\text{VL}}\}$ is generated by the VND as

$$\xi_m^{\text{VL}} = \sum_n \xi_n^{\text{CV}} \tag{16}$$

where the subscript n represents the edge index and the sum is over all edges connected to the variable node m. The message $\boldsymbol{\xi}^{\text{VL}}$ is then used to refine the LMMSE detection outputs in the next iteration (see (9)).

With the above schedule, the messages $\boldsymbol{\xi}^{\text{LV}}$, $\boldsymbol{\xi}^{\text{VC}}$, $\boldsymbol{\xi}^{\text{CV}}$, and $\boldsymbol{\xi}^{\text{VL}}$ are updated in sequence during each iteration. The iterative detection continues until convergence. This schedule is also adopted in [14].

4. Performance Analysis based on EXIT Charts

4.1 Modeling LLR with i.i.d. Gaussian Assumption

Following [2], [4], we assume that the LLRs in each message in Fig. 1(c) are i.i.d. Gaussian random variables, satisfying the consistency condition [2]. By doing this, a message can be characterized by the individual statistics of each entry.

Let ξ be an LLR in a message and x the corresponding BPSK signal. Under the above assumption, ξ can be modeled as [c.f., (9), (10) in 2]

$$\xi = (\sigma^2/2)x + \sigma\varepsilon \tag{17}$$

where ε is an independent Gaussian random variable with zero mean and unit variance. The mutual information between x and ξ is given by [2]

$$I = J(\sigma) \equiv 1 - \int_{-\infty}^{+\infty}\frac{e^{-(t-\sigma^2/2)^2/2\sigma^2}}{\sqrt{2\pi}\sigma}\log_2(1+e^{-t})dt. \tag{18}$$

With (18), we can compute the mutual information for every message in Fig. 1(c) under the i.i.d. Gaussian assumption. This is shown in Fig. 2, where the superscripts are used to indicate the corresponding relationship between the mutual information and the messages. For example, I^{LV} corresponds to $\boldsymbol{\xi}^{\text{LV}}$.

Following [2] and [4], we adopt the so-called EXIT functions to characterize the behavior of these local detectors, as discussed in the next three subsections.

4.2 Characterization of the LMMSE Detector

Let $I^{\text{LV}} = \chi(I^{\text{VL}})$ be the EXIT function of the LMMSE detector. It can be derived as follows.

From (15), we have

$$I^{\text{LV}} = J(\sigma^{\text{LV}}) = J(2\sqrt{\rho^{\text{LV}}}) = J(2\sqrt{\phi(\overline{v})}) \tag{19}$$

where the first equality follows from (18) and second equality follows from (17) in [21].

Combining (9) and (10), and letting $N \to \infty$, we have

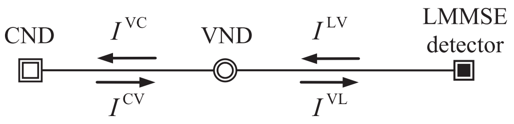

Fig. 2 Mutual information characterization for Fig. 1(c).

$$\bar{v} = 1 - \frac{1}{NM_T}\sum_{n=1}^{NM_T}\tanh^2(\xi_n^{\mathrm{VL}}/2) \tag{20a}$$

$$\to 1 - \int_{-\infty}^{+\infty}\frac{e^{-t^2/2}}{\sqrt{2\pi}}\tanh^2\left(\frac{(\sigma^{\mathrm{VL}})^2}{4}+\frac{\sigma^{\mathrm{VL}}}{2}t\right)dt \tag{20b}$$

$$\equiv T(\sigma^{\mathrm{VL}}) \tag{20c}$$

where (20b) follows from the model in (17), and σ^{VL} in (20c) is given by (using $J(\cdot)$ in (18))

$$\sigma^{\mathrm{VL}} = J^{-1}(I^{\mathrm{VL}}). \tag{21}$$

Combining (19), (20) and (21), for $N \to \infty$, we have

$$I^{\mathrm{LV}} = \chi(I^{\mathrm{VL}}) \equiv J\left(2\sqrt{\phi\left(T\left(J^{-1}(I^{\mathrm{VL}})\right)\right)}\right). \tag{22}$$

The analytic form of the EXIT function in (22) provides conventions for our precoder design as to be discussed in 6.3.

4.3 Characterization of the VND and CND

The EXIT functions for the VND and CND are denoted by (see Fig. 2)

$$I^{\mathrm{VC}}=\lambda(I^{\mathrm{CV}}, I^{\mathrm{LV}}),\ I^{\mathrm{VL}}=\eta(I^{\mathrm{CV}}),\ \text{and } I^{\mathrm{CV}}=g(I^{\mathrm{VC}}). \tag{23}$$

These EXIT functions are determined by the degree distributions of an LDPC code [4]. For a (d_l, d_r) regular LDPC code, we have

$$\lambda(I^{\mathrm{CV}}, I^{\mathrm{LV}}) \equiv J\left(\sqrt{(d_l-1)\left[J^{-1}(I^{\mathrm{CV}})\right]^2+\left[J^{-1}(I^{\mathrm{LV}})\right]^2}\right) \tag{24}$$

$$\eta(I^{\mathrm{CV}}) \equiv J\left(\sqrt{d_l}J^{-1}(I^{\mathrm{CV}})\right) \tag{25}$$

$$g(I^{\mathrm{VC}}) \equiv 1 - J\left((d_r-1)^{-1}J^{-1}(1-I^{\mathrm{VC}})\right). \tag{26}$$

4.4 EXIT Chart Analysis

The flow-graph in Fig. 3(a) summarizes the EXIT functions in (22), (24), (25) and (26). We can combine the VND and LMMSE detector in Fig. 3(a) into an overall functional block, as marked by "G-VND" (standing for generalized VND) in Fig. 3(b). The latter involves two EXIT functions, namely $g(\cdot)$ in (26) and

$$f(I^{\mathrm{CV}}) \equiv \lambda\left(I^{\mathrm{CV}}, \chi\left(\eta(I^{\mathrm{CV}})\right)\right). \tag{27}$$

Based on Fig. 3(b), we can predict the performance of the iterative receiver as follows. Denote by the subscript "q" the iteration number. We initialize $I_0^{\mathrm{CV}} = 0$, which implies no *a priori* information from the CND to the G-VND at the beginning of the iterative detection process. The mutual information during the iterative process can be tracked as

$$I_q^{\mathrm{VC}} = f(I_{q-1}^{\mathrm{CV}}),\ \text{and } I_q^{\mathrm{CV}} = g(I_q^{\mathrm{VC}})\ q = 1, \ldots, Q. \tag{28}$$

At the end of the iterative process, I_Q^{VC} and I_Q^{CV} are used to predict the bit error rate (BER) and frame error rate (FER) performance [2], [16], [21].

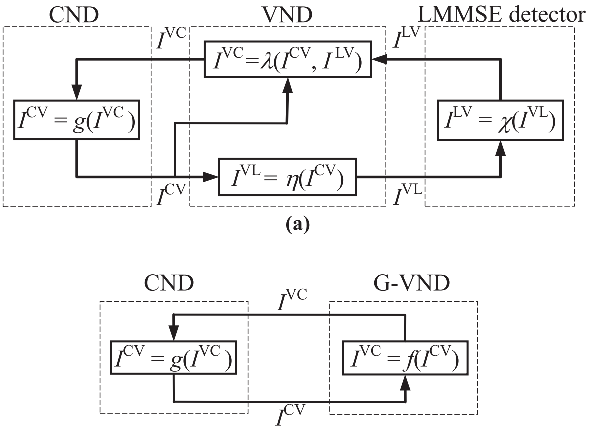

(a)

(b)

Fig. 3 (a) Flow-graph for EXIT functions. (b) An equivalent form of (a).

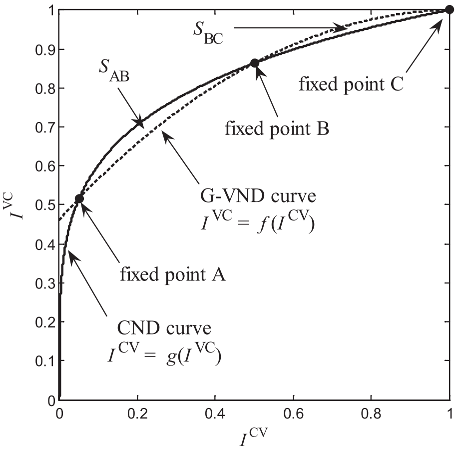

Fig. 4 An EXIT chart with three fixed points.

The behavior of the iterative process in (28) can be demonstrated by an EXIT chart as shown in Fig. 4. It is wanted that the iterative process converges to $I^{\mathrm{CV}} = 1$ and $I^{\mathrm{VC}} = 1$, (i.e., point C in Fig. 4), which represents error free detection. However, there can be multiple fixed points in an EXIT chart, such as the example with three fixed points labeled by "A", "B" and "C" in Fig. 4. In this case, the iterative process will converge to the first fixed point, i.e., point A in Fig. 4. This indicates potential detection error. We will return to this issue later in 5.3.

We can increase the transmit power to avoid the situation of multiple fixed points. However, this incurs loss in power efficiency.

4.5 Mismatch between EXIT Curves

It has been shown that near capacity performance can be achieved if the following matching condition is fulfilled [3], [20], [22]

$$f(I^{\mathrm{CV}}) = g^{-1}(I^{\mathrm{CV}}) \quad 0 \le I^{\mathrm{CV}} \le 1 \tag{29}$$

where $g^{-1}(\cdot)$ is the inverse function of $g(\cdot)$.

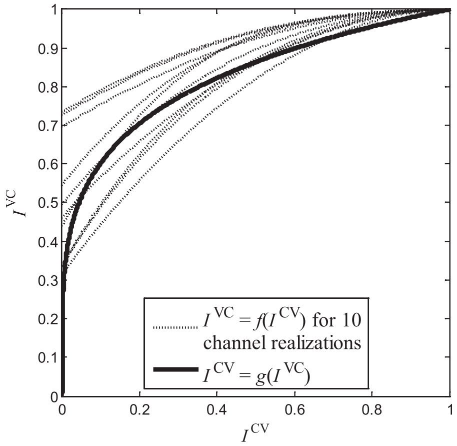

Fig. 5 An EXIT chart for 10 channel realizations.

In (29), $g(\cdot)$ is determined by the check node degree distribution of an LDPC code (see (26)) but $f(\cdot)$ is determined by the variable node degree distribution of an LDPC code as well as the channel (see (15), (23), (24), (25) and (27)).

In the case of full CSIT, we can design the precoder according to the matching condition in (29) as to be discussed in 6.1. Alternatively, we can also tune the degree distributions of the LDPC codes [3], [5], [20]. Both methods lead to excellent performance.

Without perfect CSIT, the matching condition in (29) cannot be satisfied by optimizing the degree distributions of the LDPC code or the precoder structure. This is because, as mentioned above, $f(\cdot)$ is a function of the channel matrix $\boldsymbol{H}$, as illustrated in Fig. 5. Here, the EXIT curves are generated using a (3, 6) LDPC code and 10 random realizations of a 2×2 MIMO Rayleigh fading channel. For different channel realizations, $f(\cdot)$ varies noticeably while $g(\cdot)$ remains fixed as discussed above. This clearly demonstrates the main difficulty in meeting the matching condition in (29): without accurate CSIT, $f(\cdot)$ is uncertain at the transmitter. This mismatching problem may lead to noticeable performance loss.

5. Spatial Coupling

5.1 Spatial Coupling Principle

In this section, we adopt the spatial coupling approach proposed in [13] to mitigate the mismatching problem as mentioned in 4.5.

The basic principle of spatial coupling is illustrated in Fig. 6. Due to space limitation, our discussion below is very brief. For details, please refer to [13].

In Fig. 6(a), we create L parallel copies of the system in Fig. 1(c). Each copy is referred to as a “position”. At each position, the edges between the check nodes and the variable nodes are randomly and uniformly divided into w edge subsets ($w < L$) indexed by k, $k = 0, \dots, w-1$. In Fig. 6(a), $w = 3$ and each edge subset is represented by a line between the white double circle and the white double square. Note that the variable nodes are only connected to the check nodes at the same position in Fig. 6(a).

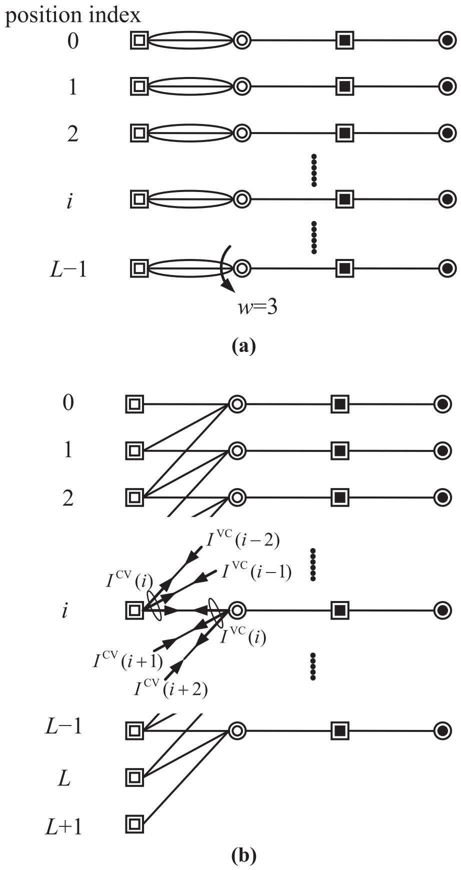

Fig. 6 Spatial coupling principle. (a) Edge grouping. (b) Edge reconnection and mutual information characterization.

In Fig. 6(b), we perform spatial coupling as follows. The variable nodes at each position i are reconnected to the check nodes at w positions (from i to $i + w - 1$) through w edge groups, respectively. Extra check nodes are created at $w-1$ positions for spatial coupling termination. This results in the factor graph of a spatially coupled LDPC (SC-LDPC) code.

Assume that a (d_l, d_r) regular LDPC code is used at each position. The resultant spatially coupled LDPC code is referred to as a (d_l, d_r, L, w) SC-LDPC code [13].

It has been demonstrated that SC-LDPC codes can achieve excellent performance in nonfading channels. See [12]–[14] and references therein. In what follows, we will show that SC-LDPC codes can be used in fading MIMO channels to handle the EXIT curve mismatching problem discussed in 4.5.

The message passing detection algorithm for the SC-LDPC coded MIMO system can be carried out using the factor graph in Fig. 6(b) in a straightforward way.

5.2 EXIT Chart Analysis for a Spatially Coupled System

The EXIT chart analysis technique can be extended to the spatially coupled system in Fig. 6(b). Let us focus on position i in Fig. 6(b). Here the mutual informations are indexed by the position number, i.e., $I^{\mathrm{CV}}(i)$ and $I^{\mathrm{VC}}(i)$.

The nodes in Fig. 6(b) can still be characterized by $g(\cdot)$ and $f(\cdot)$ in (26) and (27). The key point is that each incoming message is a uniform mixture of LLRs from different positions with different mutual information values (see Fig. 6). We can thus use the average mutual information to characterize the incoming messages. For the G-VND and CND at position i, the input average mutual informations are given by

$$\frac{1}{w}\sum_{k=0}^{w-1} I^{\mathrm{CV}}(i+k), \text{ and } \frac{1}{w}\sum_{k=0}^{w-1} I^{\mathrm{VC}}(i-k). \tag{30}$$

Following [13], we impose boundary constraints $I^{\mathrm{VC}}(i) = 1$ for $i < 0$ or $i \geq L$. Based on (26), (27) and (30), we have

$$I^{\mathrm{VC}}(i) = f\left(\frac{1}{w}\sum_{k=0}^{w-1} I^{\mathrm{CV}}(i+k)\right) \tag{31}$$

$$I^{\mathrm{CV}}(i) = g\left(\frac{1}{w}\sum_{k=0}^{w-1} I^{\mathrm{VC}}(i-k)\right). \tag{32}$$

Again, denote by q the iteration number. We initialize $I_0^{\mathrm{CV}}(i) = 0$, for $0 \leq i < L + w - 1$. For $1 \leq q \leq Q$, we track the mutual informations during the iterative process as

$$\begin{cases} I_q^{\mathrm{VC}}(i) = f\left(\frac{1}{w}\sum\limits_{k=0}^{w-1} I_{q-1}^{\mathrm{CV}}(i+k)\right) & 1 \leq i < L \\ I_q^{\mathrm{VC}}(i) = 1 & i < 0 \text{ or } i \geq L \\ I_q^{\mathrm{CV}}(i) = g\left(\frac{1}{w}\sum\limits_{k=0}^{w-1} I_q^{\mathrm{VC}}(i-k)\right) & 1 \leq i < L+w-1 \end{cases}. \tag{33}$$

The results of the above recursion can be used to predict system performance.

5.3 Area Property

Assume that there are multiple fixed points in an EXIT chart for an LDPC coded system without spatial coupling. The iterative process in (28) then converges to the first fixed point, which is not desirable as we discussed before.

With spatial coupling, interestingly, we observed that the iterative process in (33) may converge to the correct decision, i.e., $I_q^{\mathrm{CV}}(i) \to 1$ and $I_q^{\mathrm{VC}}(i) \to 1$, even the EXIT chart for the system in each position before spatial coupling has multiple fixed points. We have conducted a large amount of experiments. We observed that for $L \gg w \gg 1$, $I_q^{\mathrm{CV}}(i) \to 1$ and $I_q^{\mathrm{VC}}(i) \to 1$ if $S_{\mathrm{AB}} < S_{\mathrm{BC}}$, where S_{AB} and S_{BC} are the areas of the two regions as shown in Fig. 4. We conjecture that this property is true for general cases. We are now working on a rigorous proof of this conjecture.

Based on the above conjecture, we have a simple method to predict the performance of a spatially coupled system. Given a channel realization, assuming that there are only three fixed points as shown in Fig. 4, we can shift $f(\cdot)$ by tuning transmission power P_T. Thus S_{AB} and S_{BC} can be expressed as functions of P_T, i.e., $S_{\mathrm{AB}}(P_T)$ and $S_{\mathrm{BC}}(P_T)$.

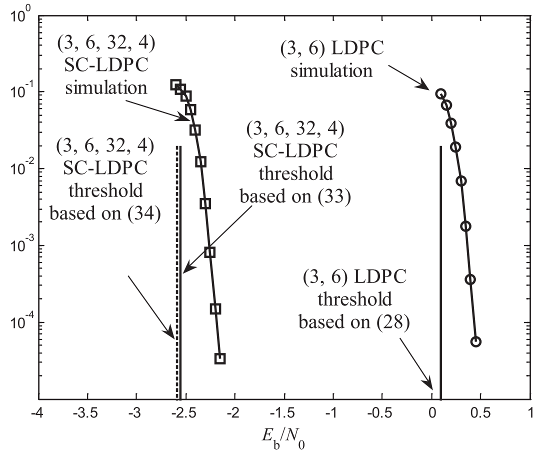

Fig. 7 BER performance and thresholds for a 2 × 2 fixed fading MIMO system with (3, 6) LDPC coding and (3, 6, 32, 4) SC-LDPC coding.

The value of P_T that results in

$$S_{\mathrm{AB}}(P_T) = S_{\mathrm{BC}}(P_T) \tag{34}$$

is used as the threshold for error-free performance for the given channel realization.

We use a numerical example to support the conjecture. Consider a 2 × 2 *fixed* fading MIMO system with

$$\boldsymbol{H}' = \begin{bmatrix} -1.749+0.927\sqrt{-1} & -0.857-1.204\sqrt{-1} \\ -0.319+0.480\sqrt{-1} & -0.109-0.006\sqrt{-1} \end{bmatrix}. \tag{35}$$

We compare the performance of a (3, 6) LDPC code and a (3, 6, 32, 4) SC-LDPC code, both with length 2^{17}. Figure 7 shows the simulated BER performance. Clearly, spatial coupling leads to performance gain of about 2.5 dB. The thresholds calculated using the EXIT functions based on (29), (33) and using the area property based on (34) are also included for comparison. Notice that the threshold based on (33) is for $w = 4$ and $L = 32$, while the threshold based on (34) is for $L \gg w \gg 1$. Their difference is very small, which provides a useful evidence for the conjecture.

6. Precoder Design with Perfect and Partial CSIT

6.1 Perfect CSIT Case

The discussions so far have been on systems without CSIT. We now consider more general cases with CSIT. We first assume that CSIT is perfect ($\alpha = 1$) so $\boldsymbol{H}$ is accurately known at the transmitter. Following [16], we can modify the precoder in (7) to the following form

$$\boldsymbol{P} = \boldsymbol{V}\boldsymbol{W}^{1/2}\boldsymbol{\Pi}\boldsymbol{F} \tag{36}$$

where $\boldsymbol{V}$ is the beamforming matrix obtained using the SVD $\boldsymbol{H}=\boldsymbol{U}\boldsymbol{D}\boldsymbol{V}^H$, $\boldsymbol{W}$ is a diagonal matrix representing power allocation, $\boldsymbol{\Pi}$ and $\boldsymbol{F}$ are the same as those in (7). In principle, the diagonal entries of $\boldsymbol{W}$ have a water-filling effect [16]. Roughly speaking, the use of $\boldsymbol{W}$ allocates more energy to channel directions with high gains and vise versa. An optimization procedure for $\boldsymbol{W}$ can be found in [16].

6.2 Partial CSIT Case

We now consider CSIT uncertainty ($\alpha < 1$). For $\alpha = 0$, the precoder structure in (7) is adopted. To facilitate our discussion below, we rewrite (7) as

$$\boldsymbol{P} = \boldsymbol{V} \cdot \boldsymbol{I} \cdot \boldsymbol{\Pi F} \tag{37}$$

where $\boldsymbol{V}$ can be an arbitrary unitary matrix. It is easy to see that $\boldsymbol{V}$ and $\boldsymbol{I}$ in (37) will not affect the performance.

For $0 < \alpha < 1$, we do not have the optimal solution in this case, so we consider the following heuristic option. Let the SVD of $\overline{\boldsymbol{H}}$ be $\overline{\boldsymbol{H}} = \overline{\boldsymbol{UDV}}^H$. We first pretend that the CSIT is perfect and $\boldsymbol{H} = \overline{\boldsymbol{H}}$ (i.e., we ignore the uncertain part $\boldsymbol{H}_W$.) Then the method outlined in 6.1 can be used to design a precoder structure below

$$\boldsymbol{P} = \overline{\boldsymbol{VW}}^{1/2} \boldsymbol{\Pi F} \tag{38}$$

where two upper hyphens "$^-$" are added on $\boldsymbol{V}$ and $\boldsymbol{W}$ to emphasize that they are obtained using the SVD of $\overline{\boldsymbol{H}}$ rather than $\boldsymbol{H}$. Note that $\boldsymbol{H}_W$ is ignored in this design so the precoder structure in (38) may not be reliable.

On the other hand, we can also assume no CSIT and ignore the available information $\overline{\boldsymbol{H}}$. Then, again, we have the precoder in (37).

We combined the two precoders in (37) and (38) as

$$\boldsymbol{P} = \overline{\boldsymbol{V}}(\beta_1 \boldsymbol{I} + \beta_2 \overline{\boldsymbol{W}})^{1/2} \boldsymbol{\Pi F} \tag{39}$$

where β_1 and β_2 are two nonnegative weight coefficients to be optimized. Intuitively, $\overline{\boldsymbol{W}}$ in (39) has the water-filling effect as mentioned in 6.1, since $\overline{\boldsymbol{H}}$ can still provide information (though imperfect) about the channel condition. Also, the term $\boldsymbol{I}$ in (39) represents a diversity effect against CSIT uncertainty.

We obtain the weight coefficients in (39) using a two-dimensional search. The EXIT chart analysis outlined in Sect. 4 provides a fast means for this purpose.

Provided that the CSIT is imperfect, the condition in (29) cannot be guaranteed in general, thus the mismatching problem demonstrated in Fig. 5 still exists for the precoder in (39). Again, spatial coupling can be applied to treat the problem, as shown in the next subsection.

6.3 Numerical Results

We now present simulation results to demonstrate the performance of the precoder in (39). The simulation settings are as follows. The MIMO channel is quasi-static Rayleigh fading with $M_R = M_T = 4$. The signaling method is QPSK with Gray mapping [19]. An underlying (3, 6) regular LDPC code is used with and without spatial coupling. The coding length is 2^{17} for both cases.

The simulated FER performance is shown in Fig. 8. In the case of no CSIT ($\alpha = 0$), there is a gain of about 2 dB between the systems with and without spatial coupling. This gain is verified by EXIT chart analysis based on the area property discussed in 5.3. We can observe that there is still about 0.7 dB gap between the system with spatial coupling and the outage performance. We believe that this gap can be reduced by carefully designing the degree distributions of the SC-LDPC code.

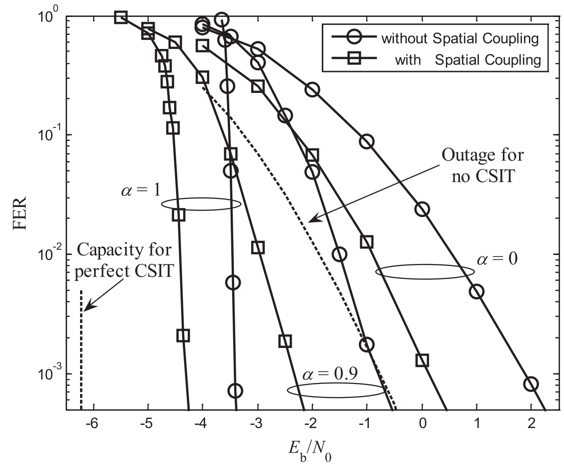

Fig. 8 FER performance for a 4 × 4 Rayleigh fading MIMO system with (3, 6) LDPC coding and (3, 6, 32, 4) SC-LDPC coding.

In the case of perfect CSIT ($\alpha = 1$), the precoder in (39) can provide an extra gain (compared with the no CSIT case) of about 5.5 dB (at FER = 10^{-3}) for the system without spatial coupling and about 4.5 dB for the system with spatial coupling. We can further observe that in the perfect CSIT case, the spatial coupling gain is about 1 dB, which is less than that in the no CSIT case. Furthermore, there is a gap of about 2 dB between the system with spatial coupling and the capacity. We are seeking for a solution for further improvement.

In the case of partial CSIT ($\alpha = 0.9$), the precoder in (39) performs between the two extreme cases of no CSIT and perfect CSIT. Again, in this case, spatial coupling provides noticeable gain.

7. Conclusions

We developed a combined scheme involving LDPC coding, linear precoding and spatial coupling. We derived an analytical method to evaluate the performance based on EXIT functions. We also observed an area property for a spatially coupled system, indicating that error-free decoding can be achieved even the underlying uncoupled system has multiple fixed points in its EXIT chart. This property is very useful to alleviate the uncertainty in partial CSIT which leads to difficulty designing LDPC codes based on the EXIT curve matching technique. Numerical results show that the proposed scheme can achieve excellent performance in MIMO channels with partial CSIT.

References

[1] S. ten Brink, "Convergence of iterative decoding," Electron. Lett.,

vol.35, no.10, pp.806–808, May 1999.

[2] S. ten Brink, "Convergence behavior of iteratively decoded parallel concatenated codes," IEEE Trans. Commun., vol.49, no.10, pp.1727–1737, Oct. 2001.

[3] A. Ashikhmin, G. Kramer, and S. ten Brink, "Extrinsic information transfer functions: Model and erasure channel properties," IEEE Trans. Inf. Theory, vol.50, no.11, pp.2657–2673, Nov. 2004.

[4] S. ten Brink, G. Kramer, and A. Ashikhmin, "Design of low-density parity-check codes for modulation and detection," IEEE Trans. Commun., vol.52, no.4, pp.670–678, April 2004.

[5] T. Richardson and R. Urbanke, Modern Coding Theory, Cambridge University Press, 2008.

[6] R.G. Gallager, "Low-density parity-check codes," IEEE Trans. Inf. Theory, vol.IT-8, no.1, pp.21–28, Jan. 1962.

[7] D.J.C. MacKay and R.M. Neal, "Near Shannon limit performance of low density parity check codes," Electron. Lett., vol.32, no.18, pp.1645–1646, Aug. 1996.

[8] C. Berrou, A. Glavieux, and P. Thitimajshima, "Near Shannon limit error-correcting coding and decoding: Turbo codes," Proc. ICC'93, pp.1064–1070, Geneva, Switzerland, May 1993.

[9] D. Tse and P. Viswanath, Fundamentals of Wireless Communication, Cambridge University Press, 2005.

[10] A. Goldsmith, S.A. Jafar, N. Jindal, and S. Vishwanath, "Capacity limits of MIMO channels," IEEE J. Sel. Areas Commun., vol.21, no.5, pp.684–702, June 2003.

[11] S.M. Kay, Fundamentals of Statistical Signal Processing: Estimation Theory, Prentice-Hall, New Jersey, 1993.

[12] A. Pusane, R. Smarandache, P. Vontobel, and J.D.J. Costello, "Deriving good LDPC convolutional codes from LDPC block codes," IEEE Trans. Inf. Theory, vol.55, no.6, pp.2577–2598, Feb. 2011.

[13] S. Kudekar, T. Richardson, and R. Urbanke, "Threshold saturation via spatial coupling: Why convolutional LDPC ensembles perform so well over the BEC," IEEE Trans. Inf. Theory, vol.57, no.2, pp.803–834, Feb. 2011.

[14] A. Yedla, P. Nguyen, H. Pfister, and K. Narayanan, "Spatially-coupled codes and threshold saturation on intersymbol-interference channels," http://arxiv.org/abs/1107.3253, 2011.

[15] S. Venkatesan, S. Simon, and R. Valenzuela, "Capacity of a Gaussian MIMO channel with nonzero mean," Proc. IEEE VTC., vol.3, pp.1767–1771, Oct. 2003.

[16] X. Yuan, C. Xu, L. Ping, and X. Lin, "Precoder design for multiuser MIMO ISI channels based on iterative LMMSE detection," IEEE J. Sel. Top. Signal Process., vol.3, no.6, pp.1118–1128, Dec. 2009.

[17] F.R. Kschischang, B.J. Frey, and H.-A. Loeliger, "Factor graphs and the sum-product algorithm," IEEE Trans. Inf. Theory, vol.47, no.2, pp.498–519, Feb. 2001.

[18] H.-A. Loeliger, J. Dauwels, J. Hu, S. Korl, L. Ping, and F.R. Kschischang, "The factor graph approach to model-based signal processing," Proc. IEEE, June 2007.

[19] J. Proakis, Digital Communications, 4th ed., McGraw-Hill, 2000

[20] X. Yuan, L. Ping, and A. Kavcic, "Achievable rates of coded MIMO systems with linear precoding and iterative linear MMSE detection," submitted to IEEE Trans. Inf. Theory.

[21] X. Yuan, Q. Guo, X. Wang, and L. Ping, "Evolution analysis of low-cost iterative equalization in coded linear systems with cyclic prefixes," IEEE J. Sel. Areas Commun., vol.26, no.2, pp.301–310, Feb. 2008.

[22] K. Bhattad and K.R. Narayanan, "An MSE-based transfer chart for analyzing iterative decoding schemes using a Gaussian approximation," IEEE Trans. Inf. Theory, vol.53, no.1, pp.22–38, Jan. 2007.

Appendix

In this appendix, we derive (12). Denote by $\boldsymbol{a}_m$ the m-th column vector of $\boldsymbol{A}$. The *extrinsic* LLR ξ_m^{LV} is given by (c.f. (4b) in [21])

$$\xi_m^{\mathrm{LV}} = 2\frac{\boldsymbol{a}_m^H\boldsymbol{R}^{-1}(\boldsymbol{r}-\boldsymbol{A}\overline{\boldsymbol{x}}) + \boldsymbol{a}_m^H\boldsymbol{R}^{-1}\boldsymbol{a}_m\overline{x}_m}{1-\overline{v}\boldsymbol{a}_m^H\boldsymbol{R}^{-1}\boldsymbol{a}_m} \tag{A$\cdot$1a}$$

$$= 2\left(\frac{\boldsymbol{a}_m^H\boldsymbol{R}^{-1}(\boldsymbol{r}-\boldsymbol{A}\overline{\boldsymbol{x}})}{1-\overline{v}\boldsymbol{a}_m^H\boldsymbol{R}^{-1}\boldsymbol{a}_m} + \frac{1}{\overline{v}}\frac{\overline{x}_m}{1-\overline{v}\boldsymbol{a}_m^H\boldsymbol{R}^{-1}\boldsymbol{a}_m} - \frac{\overline{x}_m}{\overline{v}}\right) \tag{A$\cdot$1b}$$

$$= 2\left(\frac{\overline{x}_m + \overline{v}\boldsymbol{a}_m^H\boldsymbol{R}^{-1}(\boldsymbol{r}-\boldsymbol{A}\overline{\boldsymbol{x}})}{\overline{v}(1-\overline{v}\boldsymbol{a}_m^H\boldsymbol{R}^{-1}\boldsymbol{a}_m)} - \frac{\overline{x}_m}{\overline{v}}\right). \tag{A$\cdot$1c}$$

From (11) and (13), we have

$$\hat{x}_m = \overline{x}_m + \overline{v}\boldsymbol{a}_m^H\boldsymbol{R}^{-1}(\boldsymbol{r}-\boldsymbol{A}\overline{\boldsymbol{x}}) \tag{A$\cdot$2}$$

$$\Omega_{m,m} = \overline{v} - \overline{v}^2\boldsymbol{a}_m^H\boldsymbol{R}^{-1}\boldsymbol{a}_m. \tag{A$\cdot$3}$$

Substituting (A$\cdot$2) and (A$\cdot$3) into (A$\cdot$1c), we obtain (12).

Zhonghao Zhang received the B.S. and M.S. degrees in Electrical Engineering from University of Electronic Science and Technology of China in 2005 and 2008, respectively. He is currently pursuing the Ph.D. degree at City University of Hong Kong. His research interests span the areas of iterative detection and information theory.

Chongbin Xu received the B.E. degree from Xian Jiaotong University in 2005, and the Ph.D. degree from the Department of Electronic Engineering in Tsinghua University, Beijing, China. He is currently working at the City University of Hong Kong. His research interests include iterative detection, transceiver design of MIMO systems.

Li Ping (S'87-M'91-SM'06-F'09) received his Ph.D. degree at Glasgow University in 1990. He lectured at Department of Electronic Engineering, Melbourne University, from 1990 to 1992, and worked as a research staff at Telecom Australia Research Laboratories from 1993 to 1995. He has been with the Department of Electronic Engineering, City University of Hong Kong, since January 1996 where he is now a chair professor. Dr. Li Ping received a British Telecom — Royal Society Fellowship in 1986, the IEE J.J. Thomson premium in 1993 and a Croucher Foundation Award in 2005. He is now serving as a member of Board of Governors of IEEE Information Theory Society from 2010 to 2012 and is a fellow of IEEE. His research interests include iterative signal processing, mobile communications, coding and modulation, information theory and numerical methods.